First-principles calculations of X-ray absorption spectra at the K-edge of 3d transition metals: an electronic structure analysis of the pre-edge

Delphine Cabaret, Amélie Bordage, Amélie Juhin, Mounir Arfaoui, Emilie Gaudry

HAL Id: hal-00977994

https://hal.science/hal-00977994

Submitted on 20 Oct 2014

This paper is published as part of a *PCCP* themed issue on recent developments in X-ray absorption spectroscopy

Guest Editor: Jeroen Anton van Bokhoven

Spatially resolved 3D micro-XANES by a confocal detection scheme

Geert Silversmit, Bart Vekemans, Sergey Nikitenko, Sylvia Schmitz, Tom Schoonjans, Frank E. Brenker and Laszlo Vincze, *Phys. Chem. Chem. Phys.*, 2010

DOI: 10.1039/c004103n

Wavelet transform EXAFS analysis of mono- and dimolybdate model compounds and a Mo/HZSM-5 dehydroaromatization catalyst

Robert O. Savinelli and Susannah L. Scott, *Phys. Chem. Chem. Phys.*, 2010

DOI: 10.1039/b926474d

Electronic structure of alumina-supported monometallic Pt and bimetallic PtSn catalysts under hydrogen and carbon monoxide environment

Jagdeep Singh, Ryan C. Nelson, Brian C. Vicente, Susannah L. Scott and Jeroen A. van Bokhoven, *Phys. Chem. Chem. Phys.*, 2010

DOI: 10.1039/c000403k

Determination of CO, H_2O and H_2 coverage by XANES and EXAFS on Pt and Au during water gas shift reaction

Neng Guo, Bradley R. Fingland, W. Damion Williams, Vincent F. Kispersky, Jelena Jelic, W. Nicholas Delgass, Fabio H. Ribeiro, Randall J. Meyer and Jeffrey T. Miller, *Phys. Chem. Chem. Phys.*, 2010

DOI: 10.1039/c000240m

Complementarity between high-energy photoelectron and L-edge spectroscopy for probing the electronic structure of 5d transition metal catalysts

Toyli Anniyev, Hirohito Ogasawara, Mathias P. Ljungberg, Kjartan T. Wikfeldt, Janay B. MacNaughton, Lars-Åke Näslund, Uwe Bergmann, Shirlaine Koh, Peter Strasser, Lars G.M. Pettersson and Anders Nilsson, *Phys. Chem. Chem. Phys.*, 2010

DOI: 10.1039/b926414k

In situ time-resolved DXAFS for the determination of kinetics of structural changes of H-ZSM-5-supported active Re-cluster catalyst in the direct phenol synthesis from benzene and O_2

Mizuki Tada, Yohei Uemura, Rajaram Bal, Yasuhiro Inada, Masaharu Nomura and Yasuhiro Iwasawa, *Phys. Chem. Chem. Phys.*, 2010

DOI: 10.1039/c000843p

Sulfur poisoning mechanism of steam reforming catalysts: an X-ray absorption near edge structure (XANES) spectroscopic study

Yongsheng Chen, Chao Xie, Yan Li, Chunshan Song and Trudy B. Bolin, *Phys. Chem. Chem. Phys.*, 2010

DOI: 10.1039/b925910b

Peroxide-like intermediate observed at hydrogen rich condition on Pt(111) after interaction with oxygen

Janay B. MacNaughton, Lars-Åke Näslund, Toyli Anniyev, Hirohito Ogasawara and Anders Nilsson, *Phys. Chem. Chem. Phys.*, 2010

DOI: 10.1039/b926409b

First-principles calculations of X-ray absorption spectra at the *K*-edge of 3*d* transition metals: an electronic structure analysis of the pre-edge

Delphine Cabaret,*[a] Amélie Bordage,[ab] Amélie Juhin,[ac] Mounir Arfaoui[a] and Emilie Gaudry[ad]

We first present an extended introduction of the various methods used to extract electronic and structural information from the *K* pre-edge X-ray absorption spectra of 3*d* transition metal ions. The *K* pre-edge structure is then modelled for a selection of 3*d* transition metal compounds and analyzed using first-principles calculations based on the density functional theory (DFT) in the local density approximation (LDA). The selected compounds under study are presented in an ascending order of electronic structure complexity, starting with the Ti *K*-edge of rutile and anatase, and finishing with the Fe *K*-edge of the cyanomet-myoglobin. In most cases, the calculations are compared to polarized experimental spectra. It is shown that DFT-LDA methods enable us to reproduce satisfactorily the experimental features and to understand the nature of the electronic transitions involved in the pre-edge region. The limiting aspects of such methods in modelling the core–hole electron interaction and the 3*d* electron–electron repulsion are also pointed out.

1 Introduction and overview

Transition metal elements play a crucial role in coordination chemistry (catalysis, metalloproteins), Earth sciences (3*d* elements are major constituents of the Earth) and solid state physics (magnetic materials, superconductors, *etc*.). X-Ray absorption near-edge structure (XANES) spectroscopy, thanks to its chemical and orbital selectivity, is a powerful technique to obtain precise structural and electronic information of 3*d* transition metal compounds. In particular, at the *K* edge of transition metal elements, some features, which probe the 3*d* empty orbitals, arise in the pre-edge region. Thus, the pre-edge features of transition metals are related to the coordination number, oxidation state and spin state of the absorbing atom, and to the point symmetry of the absorbing atom site (see the recent review paper of Yamamoto[1]). The latter point concerning the site symmetry is essential in the sense that the pre-edge features can be interpreted using group theory. Indeed, the analyses of the pre-edge features usually make use of the character table of the irreducible representations of the absorbing atom site symmetry point group (the more often, O_h and T_d point group symmetries are considered for a six-fold and four-fold coordinated absorbing atom, respectively, even if the absorbing atom site polyhedron is not regular). The various

methods used for pre-edge analyses can be classified into two groups: the fingerprint approach and the calculations. The fingerprint approach consists of a comparison between the pre-edge spectrum of the material under study with the ones of reference model compounds, including eventually fitting procedures of the spectra by pseudo-Voigt functions.[2–4] Three kinds of theoretical approaches to calculate the *K* pre-edge are distinguished: the multielectronic approach based on the Ligand Field Multiplet theory (LFM), the single-particle (or monoelectronic) approach based on the Density Functional Theory (DFT), and the many-body Green's function methods. This paper is focused on single-particle calculations of the *K* pre-edge structure for 3*d* transition metal bearing compounds. Before presenting the outline of the paper, we first draw up an overview of various pre-edge analyses using the methods mentioned above.

Overview

In Earth and environmental sciences, the fingerprint approach is widely used to determine the oxidation state of the probed 3*d* element in complex minerals and natural/synthetic glasses. For instance, the oxidation state of Fe in synthetic and volcanic glasses has been investigated, by fitting the corresponding Fe *K* pre-edge spectra with those of reference compounds.[2] Such an analysis is based on the 2 eV chemical shift existing between the pre-edge structure of the ferrous and ferric ions in the chosen reference compounds. According to Wilke *et al.*,[3] the most useful characteristics of the Fe *K* pre-edge to determine Fe oxidation state and coordination number are the position of its centroid and its integrated intensity. By measuring the Fe *K* pre-edge of 30 model compounds, it has been established that the separation between the average pre-edge centroid positions for Fe^{2+} and Fe^{3+} is

[a] *Institut de Minéralogie et Physique des Milieux Condensés, UMR 7590 CNRS, Université Pierre et Marie Curie, Université Paris Diderot, IPGP, IRD, 140 rue de Lourmel, 75015 Paris, France. E-mail: delphine.cabaret@impmc.upmc.fr*
[b] *Laboratoire des géomatériaux et géologie de l'ingénieur, Université Paris EST, EA 4119, 5 Bd Descartes, Champs sur Marne, 77454 Noisy-Champs cedex 2, France*
[c] *Inorganic Chemistry and Catalysis, Utrecht University, Sorbonnelaan 16, 3584 CA Utrecht, The Netherlands*
[d] *Ecole des Mines de Nancy, CS 14234 Parc de Saurupt, 54042 Nancy cedex, France*

1.4 ± 0.1 eV. This result has been used to measure the average Fe oxidation state for mixed Fe^{2+}–Fe^{3+} compounds, the pre-edge structure arising between the positions of that of Fe^{2+} and Fe^{3+}. In such a way, the Fe^{3+}/Fe^{2+} ratio has been estimated in more than ten minerals containing variable/unknown amounts of Fe^{2+}/Fe^{3+} (with an accuracy of ± 10 mol% in the oxidation state determination).[3] More recently, an experimental XANES study of the oxidation state of chromium in a variety of Cr-bearing model compounds containing Cr^{2+}, Cr^{3+}, Cr^{4+}, Cr^{5+} and Cr^{6+}, in which the Cr-site symmetry is D_{4h}, O_h and/or T_d, has been reported.[4] In particular, it is shown that the centroid position of the pre-edge feature is again a better indicator of the Cr valence than the edge position. As chromium, vanadium occurs in nature under various oxidation states (*i.e.*, V^{2+}, V^{3+}, V^{4+} and V^{5+}), and vanadium K pre-edge XANES spectra vary systematically with valence state and site symmetry.[5] These V K pre-edge properties have been used to determine the valence state of vanadium in natural vanadiferrous titanomagnetites and the proportion of vanadium occurring as V^{4+} has been calculated by comparison with octahedral V^{3+} and V^{4+}.[6,7]

All the examples cited above attest to the interest of the fingerprint approach for the analysis of the pre-edge, at least in Earth and Environmental sciences. However, the pre-edge region contains much more precise information, the extraction of which requires calculations. Before introducing the theoretical approaches used to model the pre-edge, the different electronic transitions, which may occur in the K pre-edge region of transition metal elements have to be established. There are three kinds of electronic transitions used to describe the pre-edge features, as recently explained by de Groot:[8] (i) local electric quadrupole transitions (E2), $1s \rightarrow 3d$; (ii) non-local electric dipole transition (E1), $1s \rightarrow p$, where the empty p states of the absorbing atom are hybridized with the empty $3d$ states of the nearest metal neighbours *via* the p empty states of the ligands; (iii) local electric dipole transition (E1), $1s \rightarrow p$, where the empty p states of the absorbing atom are hybridized with the empty $3d$ states of the absorbing atom. In the latter, the p–d mixing is possible only if the absorbing atom site is not centrosymmetric or if the absorbing atom site centrosymmetry is broken by the atomic vibrations. The use of calculation tools enables to determine the contribution of each kind of electronic transitions to the pre-edge features. In any case, the $3d$ empty states in the transition metal elements of the compound under study are probed in the pre-edge region, either directly through E2 transitions, or indirectly through E1 transitions. The latter can be either local (intrasite) or non-local (intersite, off-site). Therefore, the final states probed in the pre-edge are rather localized states, where the electron–electron repulsion is supposed to be important. In such cases, the appropriate method to calculate the pre-edge is *a priori* the Ligand Field Multiplet (LFM) one. For instance, the remarkable work by Westre *et al.*[9] shows that the K pre-edge features of iron ions can be interpreted in the LFM approach. In this study, a fitting procedure is first used to identify the pre-edge features. The allowed multielectronic final states are then determined using the LFM theory, and the relative energies and intensities of the pre-edge features are simulated using molecular orbitals calculations based on DFT. Thanks to this methodology, a detailed understanding of the Fe K pre-edge features of ferrous and ferric model complexes (comprising tetrahedral, octahedral, and square pyramidal Fe environment, as well as low/high spin states of Fe) has been obtained. However in ref. 9, the transition matrix elements are not calculated in the LFM framework. This has been done for the first time in the case of the Fe K pre-edge by Arrio *et al.*[10] More precisely, the eigenstates of the ions and the absolute intensities of the E2 and E1 transitions involved in the K pre-edge of Fe^{2+} and Fe^{3+} in minerals, where the iron ions are either in octahedral or tetrahedral sites, have been calculated. The LFM calculated spectra of the $3d^n \rightarrow 1s^1 3d^{n+1}$ E2 transitions with a crystal field value $10Dq$ of 1.2 eV for $n = 0,\ldots,9$ have been recently reported, and it has been shown that charge-transfer effects have a weak influence on the $1s \rightarrow 3d$ pre-edge spectral shapes.[11]

Single-particle methods are quite widely used to calculate $3d$ element K pre-edge spectra, although they are in principle not fully appropriate for such applications. The analysis of the pre-edge features can be carried out by both cross-section and local density of states calculations. Single-particle calculations are performed either in a cluster approach, or using periodic boundary conditions. A cluster approach using the finite difference method of the FDMNES code[12] has been successfully used to calculate the Ti K pre-edge structure in TiO_2-rutile, providing a Mulliken-type electron population analysis of the titanium atoms (either excited or not).[13] The cluster approach of the Feff code[14] has been applied to the Mn K pre-edge, in order to distinguish the spectral signature of Mn^{2+} from the one of Mn^{3+} in Mn-bearing oxides.[15] The calculations also helped to determine the E1 contribution arising from the metal–metal pairs, as previously described in point (ii), in order to include it in the baseline that is used to extract the pre-edge features. Indeed, such E1 contributions complicate the determination of the absorbing atom oxidation state and symmetry when using fingerprint fitting procedures.[15] Similarly, Feff single-particle calculations have been performed at the Cr K-edge to support the experimental fingerprint analysis carried out on a large series of pre-edge spectra in Cr-bearing oxide minerals.[4] Next to cluster approaches, band structure codes are often used to interpret the pre-edge features. Many band structure codes now include the explicit calculation of the absorption cross-section in the electric dipole and quadrupole approximations, and several applications can be found in the literature.[16–21] Recently, a plane-wave DFT method including $GGA + U$ has been developed for XANES calculations and successfully applied to the Ni K pre-edge polarized spectra.[22] The method initially devoted to norm-conserving pseudopotentials was also extended to ultrasoft pseudopotentials.[23]

Since single-particle methods are formally dedicated to ground state calculations, many body Green's function approaches have been developed in order to model electronic excitations.[24] These approaches include time-dependent DFT (TD-DFT), GW calculations and the Bethe–Salpeter equation. TD-DFT calculations have been performed at the V K-edge of V_2O_5,[25] and at the Fe K-edge of a series of ten iron model complexes, giving a correct agreement with experiment in the pre-edge region.[26] The Bethe–Salpeter approach has been

applied to the calculation of the Ti K pre-edge structure in rutile[27] and in $SrTiO_3$.[28] Although promising, such methodologies still remain quite too challenging to be applied to complex materials.

Outline of the paper

In the following, we present various single-particle band structure calculations of the K pre-edge structure of $3d$ transition metals compounds. First, the computational details are given and then the results are presented using an ascending order of electronic interaction complexity. In the selected compounds, the $3d$ elements all sit in a distorted octahedral environment. However, a regular octahedron with O_h symmetry is considered in a first approximation, so that the $3d$ levels are split into two groups: the t_{2g} and the e_g orbitals. The various $3d$ shell occupations studied in this paper are illustrated in Fig. 1. Five distinct cases of $3d$ occupation are considered. First, the simplest case of the Ti K pre-edge in titanium oxides (rutile and anatase) will be presented. Indeed, since the formal charge of Ti in TiO_2 is $+IV$, there are no $3d$ electrons (Fig. 1a), which provides an ideal situation for single-particle calculations. Second, two examples of Fe K pre-edge where Fe is divalent ($3d^6$) in a low spin state are described. In this case, the t_{2g} orbitals are fully occupied and the e_g ones are empty (see Fig. 1b). Thus, the $3d$ states probed by X-ray absorption spectroscopy are the e_g ones only. In such a case, the photoelectron is excited to a level where the multielectronic effects are expected to be weak enough to be treated within a single-particle framework. The compounds studied are pyrite, a mineral of formula FeS_2, and a model molecule, which represents the environment of iron in carbonmonoxy–myoglobin (MbCO). Third, Cr K pre-edge single-particle calculations are presented for three insulating materials ($MgAl_2O_4$: Cr^{3+}, $Be_3Si_6Al_2O_{18}$: Cr^{3+} and α-Al_2O_3 : Cr^{3+}), in which Cr occurs as an impurity and has a $+III$ oxidation state ($3d^3$). Here, the single-particle calculations need to be spin-polarized since, in an octahedral environment, the t_{2g} orbitals of Cr^{3+} are occupied by three electrons with parallel spins (see Fig. 1c). In spin-polarized calculations, spin up and spin down transition matrix elements are calculated separately. Consequently, for spin up transitions, the situation is quite similar to that of Fe^{2+} in low spin states, in the sense that the transitions towards $3d$ states only occur towards e_g states (directly for E2 transitions or indirectly for local E1 transitions). Therefore the electron–electron interaction is supposed to be weak enough to be treated in a single-particle framework. Equally, for spin down transitions, the situation looks equivalent to the case of the Ti K pre-edge since both the t_{2g} and e_g levels are empty and can be probed through X-ray absorption spectroscopy. Finally, we present two examples that can be considered as limit cases to be treated within a single-particle approach: V^{3+} impurity in the garnet–grossular structure, and low spin Fe^{3+} in a molecule modelling the cyanomet–myoglobin protein (MbCN).

In the case of V^{3+} ($3d^2$), the t_{2g} states are occupied by two parallel spins, leaving vacant one of the three monoelectronic orbitals (see Fig. 1d). Thus, for the majority spin, the electron–electron repulsion is expected to play a significant role in the electronic structure of vanadium, which *a priori* makes the
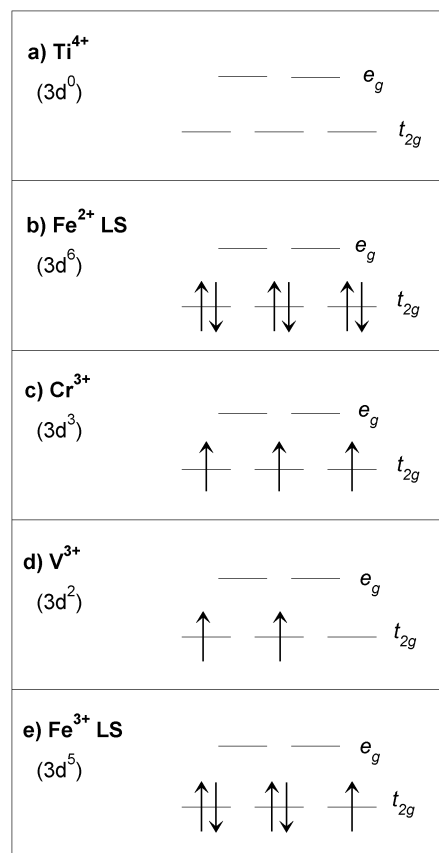
Fig. 1 Representation of the $3d$ levels electronic occupation (in O_h symmetry) of the transition metal ions investigated.

single-particle approximation too strong to be used for the transition matrix element calculation. On the contrary, for the minority spin, since both the t_{2g} and e_g orbitals are empty, the calculation of the transition matrix elements for the minority spin is *a priori* equivalent to the previous situation (Fig. 1c). The last case, corresponding to low spin Fe^{3+} ($3d^5$) in MbCN, combines the difficulties of Cr^{3+} for the majority spin and of V^{3+} for the minority spin (Fig. 1e). Hence, this last application of single-particle calculation appears to be the most critical case among all the examples treated here. For each compound, we first give the electronic transitions expected in the pre-edge region, as expected from the absorbing atom site symmetry (and crystallographic structure). Then, we compare the results of the single-particle calculations with the experimental data and finally, we give the assignment of the pre-edge features.

2   Computational details

In the monoelectronic framework, the X-ray absorption cross-section has the following general expression:

$$\sigma(\omega) = 4\pi^2 \alpha \hbar \omega \sum_f |\langle \psi_f | H_{int} | \psi_i \rangle|^2 \delta(E_i + \hbar\omega - E_f) \quad (1)$$

where α is the fine-structure constant, $\hbar\omega$ the energy of the incoming photons, $|\psi_i\rangle$ the initial state with energy E_i, and $|\psi_f\rangle$

the final state with E_f. The interaction Hamiltonian H_{int} is given by $\hat{\varepsilon}\cdot\mathbf{r}$ in the electric dipole approximation, and by $\frac{i}{2}\hat{\varepsilon}\cdot\mathbf{r}\,\mathbf{k}\cdot\mathbf{r}$ in the electric quadrupole approximation, $\hat{\varepsilon}$ and $\mathbf{k}$ being the polarization vector and the wave vector of the photon beam, respectively. In the absence of coupling between the electric dipole and quadrupole terms, the total absorption cross-section $\sigma(\omega)$ is simply the sum of electric dipole and electric quadrupole contributions, as follows:

$$\sigma(\omega;\hat{\varepsilon},\mathbf{k}) = 4\pi^2\alpha\hbar\omega\sum_f (|\langle\psi_f|\hat{\varepsilon}\cdot\mathbf{r}|\psi_i\rangle|^2$$
$$+ \frac{1}{4}|\langle\psi_f|\hat{\varepsilon}\cdot\mathbf{r}\,\mathbf{k}\cdot\mathbf{r}|\psi_i\rangle|^2)\delta(E_i + \hbar\omega - E_f). \quad (2)$$

This is the case if one uses exclusively linear polarization and if the system is time-reversal invariant or centrosymmetric.[29] The electric dipole and quadrupole cross-sections show an angular dependence, i.e. variations of the spectral features are expected when the sample orientation varies with respect to the incident X-ray beam. The anisotropy of the cross-sections depends on the crystal point group of the investigated compound and the complete dependence of each point group has been given by Brouder.[29] Note that in the case of cubic crystals, the electric dipole cross-section does not show any angular dependence.

For all the compounds except pyrite, the total cross section (eqn (2)) has been calculated within DFT codes using a plane-wave basis set, pseudopotentials and periodic boundary conditions. For pyrite, the total cross-section has been calculated with the FDMNES code,[12] using a self-consistent field (SCF) electronic potential determined within the Full-potential Linearized-Augmented plane-wave framework of the Wien2k code.[30] In each case the calculation is performed in the two following steps: (i) the determination of the SCF charge density of a supercell including the 1s core-hole on the absorbing atom, through the minimization of the total energy of the system, (ii) the computation of the absorption cross section, using the continued fraction method described in ref. 31 and 32 for the plane-wave DFT codes, and using the finite difference method for the FDMNES one.

For the minerals, the calculations were carried out from the crystallographic structures given in Table 1. For the doped minerals, the atomic positions were first relaxed in order to determine the structural modifications induced by the substitution of one aluminium atom by either one chromium in the case of Cr-doped spinel, or by one vanadium atom in the case of doped-grossular (tsavorite). The results of this relaxation step are not recalled here since they have been presented in details in ref. 21 and 33 for Cr-doped spinel and tsavorite, respectively. In the case of MbCO and MbCN, there was no need to consider the whole protein in the XANES calculation, since the mean free path of the core-electron ejected during the absorption process (i.e. the so-called photoelectron) does not exceed about ten Angström. Hence, the calculations have been performed from the 48 atom cluster shown in Fig. 2, embedded in a large cubic supercell. The cluster has been oriented within the cell in such a way that the Fe–N_p bonds are along the x and y axis, and that the Fe–N_{his} along the
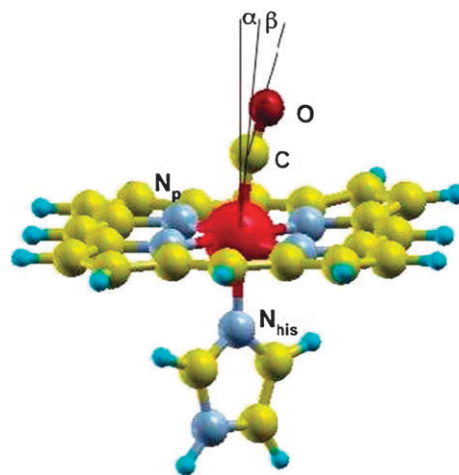
Fig. 2 Local environment of Fe in MbCO, within the cluster used for XANES calculation. It contains 48 atoms, including additional hydrogen atoms introduced to ensure the neutrality of the system. The nitrogen first neighbours of iron are labelled N_p for the four belonging to the heme plane and N_{his} for the one belonging to the H93 histidine residue. The angles α and β are introduced to characterize the angular geometry of the chain Fe–C–O (or Fe–C–N in the case of MbCN). This Figure has been generated by XCrysDen.[61]

z axis. The atomic positions are those given by Della Longa et al.[34] for MbCO and by the 2JHO protein data bank (PDB) code for MbCN.[35] The structural parameters of the Fe environment in both proteins are given in Table 2. In the case of MbCO, since the pre-edge appears to be sensitive to the bending of the Fe–C–O chain, two values of the β angle were considered (Fig. 2): 14°, as in ref. 34, and a smaller one equal to 10°.

The plane-wave DFT codes used in this study were either the PARAllel Total Energy Code[36] for Cr-doped spinel and the Quantum-Espresso suite of codes[37] (including the XSpectra package[22]) for the other compounds. Troullier–Martins[38] norm-conserving pseudopotentials in the Kleinman–Bylander form[39] have been used. The parameters used for their generation are listed in Table 3. Note that the pseudopotential of the absorbing atom is built with only one 1s electron in its electronic configuration. The computational details of the calculations (i.e., supercell size, approximation for the exchange and correlation density functional, energy cut-off, k-point grid, broadening parameter γ used in the continued fraction formulation of the cross-section and S_z value if needed) are given in Table 4. Local and partial density of states (lp-DOS) were calculated in the case of MbCO and MbCN, using Quantum-Espresso. The lp-DOS calculations, which took into account the 1s core-hole on Fe, were calculated using Löwdin projections and a Gaussian broadening of 0.07 eV. Note that in the case of MbCO, they were obtained for $\beta = 14°$. In the case of pyrite, the absorption cross section calculations have been performed for a 51 atom cluster. The SCF full-potential, generated using Wien2k, has been determined by minimizing the total energy of a $2 \times 2 \times 2$ cubic supercell, including a 1s core-hole on one of the 32 Fe atoms. The other parameters of the code were set to the default values.

Table 1 Description of the crystallographic structures of the minerals under study. The point group of the absorbing atom site is indicated. In the case of Cr-doped spinel and tsavorite, the Z value is the one of the corresponding undoped minerals

Compounds	Chem. formula	Cryst. syst.	Space group	Abs. atom site	Cell param.	Z
Rutile[55]	TiO_2	Tetragonal	$P4_2/mnm$	Ti (mmm)	$a = 4.5937$ Å $c = 2.9587$ Å	2
Anatase[55]	TiO_2	Tetragonal	$I4_1/amd$	Ti ($\bar{4}m2$)	$a = 3.7845$ Å $c = 9.5153$ Å	4
Pyrite[56]	FeS_2	Cubic	$Pa\bar{3}$	Fe ($\bar{3}$)	$a = 5.1175$ Å	4
Cr-doped spinel[57]	$MgAl_2O_4$:Cr^{3+}	Cubic	$Fd\bar{3}m$	Cr ($\bar{3}m$)	$a = 8.0806$ Å	8
Tsavorite[58]	$Ca_3Al_2(SiO_4)_3$:V^{3+}	Cubic	$Ia\bar{3}d$	V ($\bar{3}$)	$a = 11.847$ Å	8

Table 2 Structural characteristics of the local surrounding of Fe in the MbCO and MbCN clusters used for XANES calculation. Distances are in Å and angles in degrees

MbCX	$\langle d_{Fe-N_p}\rangle$	$d_{Fe-N_{his}}$	d_{Fe-C}	d_{C-X}	α	β	PDB code
MbCO[34]	2.00	2.06	1.83	1.07	6	14	/
MbCN[35]	2.04	2.08	1.92	1.11	4	13	2JHO

Table 3 Parameterization used for the generation of the norm-conserving Troullier–Martins pseudopotentials. The core radii of the valence states are indicated in parentheses in Bohr units. The Mg pseudopotential includes non linear core-correction

Atom	Valence states	Local part
H	$1s^1(1.00)$	s
C	$2s^2(1.50)\ 2p^{1.5}(1.50)$	p
N	$2s^2(1.45)\ 2p^3(1.45)$	s
O	$2s^2(1.45)\ 2p^4(1.45)$	p
Mg	$3s^2(2.00)\ 3p^0(2.00)\ 3d^0(2.00)$	d
Al	$3s^2(2.00)\ 3p^0(2.00)\ 3d^0(2.00)$	d
Si	$3s^2(2.00)\ 3p^{1.3}(2.00)\ 3d^{0.2}(2.00)$	d
Ca	$3s^2(1.45)\ 3p^6(2.00)\ 3d^0(1.45)$	d
Ti	$3s^2(1.00)\ 3p^6(1.60)\ 3d^0(1.50)$	s
V	$3s^2(1.00)\ 3p^6(1.60)\ 3d^2(1.50)$	s
Cr	$3s^2(1.00)\ 3p^6(1.70)\ 3d^3(1.70)$	d
Fe	$3s^2(1.00)\ 3p^6(1.20)\ 3d^6(1.20)$	p

3 Results and discussion

3.1 Ti K-edge

TiO$_2$-rutile. The tetragonal point group of rutile is $\frac{4}{m}mm$ (D_{4h}), which yields a dichroic behaviour of the XANES in the electric dipole approximation.[29] The point symmetry of the Ti site is mmm (D_{2h}), thus it is centrosymmetric. Consequently, local E2 transitions and non-local E1 transitions are expected to contribute to the pre-edge features.

Note that local E1 transitions due to the atomic vibrations are not formally excluded. This point will not be investigated here.

Fig. 3 shows the comparison of the calculated polarized spectra with the experimental ones of Poumellec *et al.*[40] for $\hat{\varepsilon}$ parallel and perpendicular to the 4-fold symmetry axis (*i.e.*, the z axis of the tetragonal cell), the wave vector being along the [110] direction. The theoretical spectra are calculated either with or without the core-hole. The decomposition into E1 and E2 contributions is also shown. For both polarizations, the pre-edge region exhibits three well defined features, labelled A_1, A_2 and A_3, which are reproduced by the single-particle calculations. For $\hat{\varepsilon} \parallel z$, the theoretical E2 contribution shows two peaks, which contribute to A_1 and A_2. The E1 contribution also shows two peaks, but they contribute to A_2 and A_3. Therefore, A_1 is a pure E2 peak, originating from $1s \rightarrow 3d$ local transitions. Peak A_3 is a pure E1 non-local peak, originating from $1s \rightarrow p$ transitions, where the p empty states of the absorbing atom are hybridized with empty $3d$ states of the Ti second neighbours. This hybridization is achieved *via* the empty p orbitals of the O first neighbours. Peak A_2 originates from both kinds of transitions (local E2 and non local E1), the E2 contribution representing around 10% of the E1 + E2 sum. For $\hat{\varepsilon} \perp z$, the E1 contribution also exhibits two peaks, explaining the origin of peaks A_2 and A_3, while the E2 contribution only displays one peak, giving the origin of peak A_1.

Now the question is why the E2 contribution is characterized by two peaks for $\hat{\varepsilon} \parallel z$ and only one for $\hat{\varepsilon} \perp z$, the wave vector **k** being parallel to [110]. To answer this question, one should consider the crystallographic structure of rutile. The tetragonal unit cell of rutile comprises two TiO_6 octahedra, which are crystallographically equivalent but are differently orientated with respect to the photon beam (see Fig. 4). When

Table 4 Description of the computational details of all the XANES calculations presented in this paper. The supercell of Cr-doped spinel (resp. tsavorite) contains one Cr (resp. V) impurity in substitution for one Al. In the case of MbCO and MbCN, the size of the supercell is given in Bohr.[3] In the case of spin-polarized calculation, the value of S_z imposed to the supercell is given. PBE and CA refer to the exchange and correlation density functional formulation of Perdew–Burke–Ernzerhof[59] and Ceperley-Alder,[60] respectively

Compounds	Supercell	Spin pol.	E_{xc}	Cut-off	k-point grid (SCF)	k-point grid (XANES)	γ/eV
Rutile	Tetragonal $2 \times 2 \times 3$	none	GGA-PBE	80 Ry	$1 \times 1 \times 1$	$4 \times 4 \times 4$	0.7
Anatase	Tetragonal $2 \times 2 \times 3$	none	GGA-PBE	90 Ry	$1 \times 1 \times 1$	$4 \times 4 \times 4$	0.47
Cr-doped spinel	Trigonal $2 \times 2 \times 2$	$S_z = \frac{3}{2}$	LDA-CA	70 Ry	$1 \times 1 \times 1$	$3 \times 3 \times 3$	0.54
Tsavorite	Cubic $1 \times 1 \times 1$	$S_z = 1$	LDA-CA	90 Ry	$1 \times 1 \times 1$	$4 \times 4 \times 4$	0.5
MbCO	$35 \times 35 \times 35$	None	GGA-PBE	90 Ry	$1 \times 1 \times 1$	$4 \times 4 \times 4$	0.625
MbCN	$35 \times 35 \times 35$	$S_z = \frac{1}{2}$	GGA-PBE	90 Ry	$1 \times 1 \times 1$	$4 \times 4 \times 4$	0.625
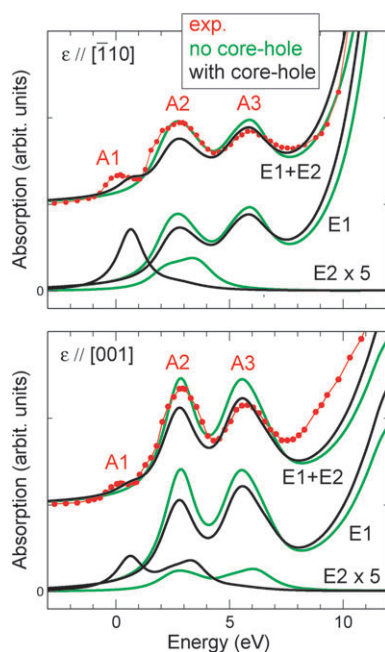
Fig. 3 Comparison between experimental (red line with circles) and calculated (solid line) Ti K pre-edge spectra of rutile, for the $\varepsilon \parallel z$ (bottom) and $\varepsilon \perp z$ (top) experimental configurations. The theoretical spectra were calculated for a supercell including a core-hole (black line) or not (green lines), in order to show the effects of the presence of the $1s$ core-hole. The zero energy corresponds to the highest occupied state of the calculation including the core-hole effects. Note that the E2 contribution has been multiplied by 5 for clarity.

both $\mathbf{k}$ and $\hat{\varepsilon}$ are between the Ti–O bonds, the E2 transition probes the local e_g-like orbital. This is the case for $\hat{\varepsilon} \parallel z$ when the site 1 is excited. On the contrary, when one of the $\mathbf{k}$ or $\hat{\varepsilon}$ vectors is between the Ti–O bonds and the other along a Ti–O bond, the electronic transition probes a local orbital between the bonds, which is mainly t_{2g}-like. This case is encountered for $\hat{\varepsilon} \parallel z$ when the site 2 is excited, and for $\hat{\varepsilon} \perp z$ when both Ti sites are excited. Therefore, when $\hat{\varepsilon} \parallel z$ (and $\mathbf{k} \parallel [110]$), while the d_{xz} and d_{yz} states of the crystal are probed, the first E2 peak corresponds to a transition from the $1s$ level to the t_{2g}-like orbital belonging to the Ti site 2, and the second E2 peak to a transition to the e_g-like orbital belonging to the Ti site 1. When $\hat{\varepsilon} \perp z$ (and $\mathbf{k} \parallel [110]$), while the $d_{x^2-y^2}$ states of the crystal are probed, the E2 peak corresponds to transitions from the $1s$ orbitals to t_{2g}-like orbitals of both Ti sites. Following similar geometrical arguments, one can observe that for the non-local E1 contributions, the t_{2g}- and e_g-like orbitals of the Ti neighbours are *indirectly* probed at the energy positions of A_2 and A_3 peaks, respectively. The energy position of the t_{2g} and e_g orbitals is different for the Ti absorbing atom and for the Ti non-excited neighbours because the $1s$ core-hole attracts the $3d$ levels of only the Ti absorbing atom (the corresponding energy shift being about 2 eV). This result is supported by the calculation, which does not take into account the core-hole effects (see green curves in Fig. 3). Indeed, the E2 contributions probing the t_{2g} and e_g levels of the non-excited Ti are located at the positions of A_2 and A_3, respectively. The assignment of the three Ti K pre-edge features of rutile for $\hat{\varepsilon} \parallel z$ and $\hat{\varepsilon} \perp z$ is summarized in Table 5. It is in total agreement with previous
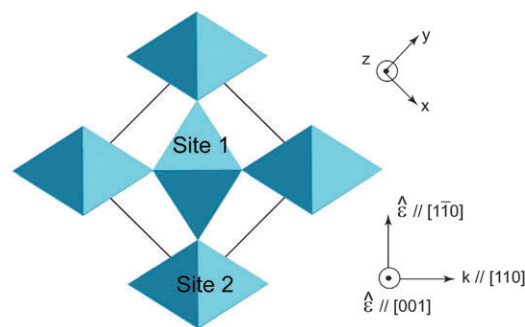
Fig. 4 Crystallographic structure of rutile, showing the orientation of the two equivalent TiO_6 octahedra in the unit cell with respect to the polarisation and wave vectors for the two experimental setups.

cluster calculations[13] performed using the fitting approach of the FDMNES code.[12]

Although the single-particle calculations enable us to establish the origin of the pre-edge features, the agreement between experiment and theory is not fully satisfactory. First, the A_1 calculated peak is located at a too high energy (about 0.6 eV), when compared to experiment. This disagreement represents the main drawback of the method used here, which takes into account the core-hole effects by self-consistently calculating the charge density for a supercell including a $1s$ core-hole on one of the Ti atoms. When no core-hole is present in the calculation (green lines), one observes that the E1 contribution is not much modified. Only the relative intensities of peaks A_2 and A_3 are changed. On the contrary, the E2 contribution is very sensitive to the core-hole effects. The presence of the core-hole especially affects the energy positions of the two local transitions $1s \rightarrow 3d\text{-}t_{2g}$ and $1s \rightarrow 3d\text{-}e_g$ by attracting them to lower energy. Without the core-hole, no peak A_1 is reproduced. Nevertheless this attractive effect does not seem sufficient to yield a total agreement with experiment. However, it also appears that if the attraction were more important, the $3d\text{-}t_{2g}$ states of the excited atom could fall in the occupied states. The presence of the core-hole dramatically affects the value of the gap, which decreases from 1.82 eV to 0.36 eV (at the Γ point) when taking into account the core-hole. Consequently, the fact that E2 peaks are at too high energy is attributed to the use of single-particle DFT formalism based on the local density approximation. Such methods are known to underestimate the gap of insulating materials, and it appears here that they are not fully appropriate to model the

Table 5 Assignment of the three A_1, A_2 and A_3 pre-edge features of the Ti K-XANES spectra of rutile for two distinct orientations of the incident photon beam polarization ($\hat{\varepsilon}$)

Peak	Assignment for $\hat{\varepsilon} \parallel z$
A_1	E2: $1s \rightarrow 3d\text{-}t_{2g}$ of Ti absorber
A_2	E1: $1s \rightarrow p_z$ hybrid. $3d\text{-}t_{2g}$ of Ti neighb. + E2: $1s \rightarrow 3d\text{-}e_g$ of Ti absorber
A_3	E1: $1s \rightarrow p_z$ hybrid. $3d\text{-}e_g$ of Ti neighb.

Peak	Assignment for $\hat{\varepsilon} \perp z$
A_1	E2: $1s \rightarrow 3d\text{-}t_{2g}$ of Ti absorber
A_2	E1: $1s \rightarrow (p_x, p_y)$ hybrid. $3d\text{-}t_{2g}$ of Ti neighb.
A_3	E1: $1s \rightarrow (p_x, p_y)$ hybrid. $3d\text{-}e_g$ of Ti neighb.

core-hole–electron interaction. The Ti K pre-edge of rutile has recently been calculated using a Bethe–Salpeter approach (BS).[27] When the core-hole–electron interaction is included, the A_1 peak appears at nearly the right position, and the overall agreement with experiment is satisfactory. Thus the BS approach provides a better description of the core-hole effects occurring in X-ray absorption. Second, the discrepancy with experiment concerns the shape of peak A_2, which seems to include two components in the experimental data. According to the measurements of Le Fèvre et al.,[41] the first component would be an E2 one ($1s \rightarrow 3d$-e_g) and the second component, an E1 one ($1s \rightarrow p$-hybridized with the t_{2g}-shell of the Ti neighbours). In the calculations presented here, these two contributions are not resolved in energy, due again to the difficulty of single-electron approach to fully account for the core-hole–electron interaction. The last discrepancy is related to the intensity of peak A_2, which is not high enough with respect to the experimental one. Atomic vibrations have been invoked to be at the origin of this discrepancy.[42,43]

TiO$_2$-anatase. The crystallographic structure of anatase is tetragonal too, with the same point group as rutile. However the Ti site symmetry is $\bar{4}m2$ (D_{2d}) and then is not centrosymmetric. Consequently, in addition to E2 and non-local E1 transitions, local E1 transitions are expected in the Ti K pre-edge region of anatase.

The Ti K pre-edge isotropic spectrum is compared to the experimental data of ref. 44. The results are shown in Fig. 5. The Ti K pre-edge of anatase is characterized by three peaks (A_1, A_2 and A_3), like in rutile. However, unlike the case of rutile, the E1 part exhibits three contributions, due to the fact that local E1 transitions also occur. The E2 contribution displays two features: a $1s \rightarrow 3d$-t_{2g} well-resolved peak followed by a broad and weak $1s \rightarrow 3d$-e_g peak. The first E2 peak represents 22% of the total intensity of peak A_1 and the second, 2% of the total intensity of peak A_2. The electric quadrupole contribution is therefore weak compared to the electric dipole one, as expected in a non-centrosymmetric site. The assignment of the three pre-edge peaks is given in Table 6.

The agreement between theory and experiment obtained for anatase is equivalent to the one of rutile, i.e., it has two main drawbacks. First, the calculated A_1 peak is at too high energy
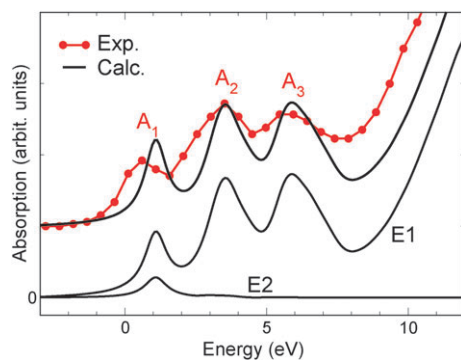
Fig. 5 Comparison between experimental (red line with circles) and calculated (black solid line) Ti K pre-edge isotropic spectra of anatase. The calculated spectrum is the sum of the E1 and E2 contributions, which are also shown.

Table 6 Assignment of the three A_1, A_2 and A_3 pre-edge features of the Ti K-XANES spectra of anatase

Peak	Assignment
A_1	E1: $1s \rightarrow p$-t_{2g} of Ti absorber
	+ E2: $1s \rightarrow 3d$-t_{2g} of Ti absorber
A_2	E1: $1s \rightarrow p$-e_g of Ti absorber
	+ E1: $1s \rightarrow p$ hybrid. $3d$-t_{2g} of Ti neighb.
	+ E2: $1s \rightarrow 3d$-e_g of Ti absorber
A_3	E1: $1s \rightarrow p_z$ hybrid. $3d$-e_g of Ti neighb.

(of about 0.5 eV). Second, the A_2 peak may contain two components, as suggested by Glatzel et al.,[45] which are not distinguishable in the simulation. These two components would come from the clear energy separation between the E2 and E1 contributions. These two drawbacks may have the same origin, i.e., the lack of DFT to properly model the core-hole–electron interaction. Indeed the second peak involves local and non-local transitions. The local ones are E1 and E2, thus involving the $3d$-e_g shell of the Ti absorbing atom. Due to the misplacements of the $3d$ levels of the excited Ti, the $3d$ states of the absorbing Ti are located at too high an energy (i.e., the core-hole is not attractive enough).

3.2 Low-spin Fe^{2+} K-edge

Carbonmonoxy-myoglobin (MbCO). Myoglobin (Mb) is a single-chain globular protein of 153 amino acids, containing a heme, i.e., a iron-containing porphyrin. A proximal histidine (H93) group is attached directly to the iron centre, and a distal histidine group on the opposite face, not bonded to the iron. When a CO molecule is linked to Fe in the vicinity of the distal histidine, the Fe ion is in a divalent low spin state. The six coordination positions of Fe are occupied, i.e., the four nitrogen atoms in the heme plane (labelled N$_p$), the nitrogen atom belonging to the distal histidine (H93), and the carbon atom of the CO molecule (see Fig. 2). The protein is then called carbonmonoxymyoglobin (MbCO). MbCO crystallizes in a monoclinic lattice (space group $P2_1$), with two molecules (about 1500 atoms) per unit cell.[46,47] The two Fe atoms contained in the unit cell obviously are too far from each other to interact. Therefore, since the Fe site is non-centrosymmetric in an approximate 4 mm (C_{4v}) symmetry, two kinds of transitions are expected in the pre-edge: E2 and local E1.

Della Longa et al. have recorded angular-dependent spectra at the Fe K-edge of a single crystal of MbCO.[48] The polarized spectra corresponding to the X-ray polarization parallel and normal to the heme plane have been deduced by neglecting the anisotropy in the heme plane.[48] Fig. 6 (top panels) compares the polarized experimental spectra with the theoretical ones in the pre-edge region. A more complete study including the XANES features will be presented in a forthcoming publication.[49] For both polarizations, the Fe K pre-edge region is characterized by two features A_1 and A_2, which are reproduced by the calculations. The E1 and E2 decomposition indicates that (i) in the case of $\hat{\varepsilon} \perp$ heme, the two peaks essentially arise from E1 transitions (the E2 transitions represent 5% of the total intensity of peak A_2), (ii) in the case of $\hat{\varepsilon} \parallel$ heme, peak A_1 and peak A_2 originate from E2 transitions and local E1 transitions, respectively. While the energy

separation between A_1 and A_2 is satisfactorily calculated (with an error of about 0.2 eV), the theoretical pre-edge is too high in energy with respect to the experimental one: the shift is about 1.4 eV for the $\hat{\varepsilon} \parallel$ *heme* configuration and 0.9 eV for the $\hat{\varepsilon} \perp$ *heme* configuration. Again, we observe that when the $3d$ orbitals of the absorbing atom are involved in the origin of the pre-edge features, the latter occur at a too high energy, when calculated in a single-particle DFT approach.

In order to further analyze the origin of the two features, the lp-DOS are also shown in Fig. 6 (bottom panels). The lp-DOS plots enable to visualise the reason why the E2 transitions are negligible when $\hat{\varepsilon} \perp$ *heme* and significant when $\hat{\varepsilon} \parallel$ *heme*. Indeed, when $\hat{\varepsilon} \perp$ *heme* (*i.e.* $\hat{\varepsilon} \parallel [001]$ and $\mathbf{k} \parallel [\bar{1}10]$), only the t_{2g} orbitals can be probed. Since they are mostly occupied, the resulting E2 absorption cross-section is found very weak. On the contrary, when $\hat{\varepsilon} \parallel$ *heme* (*i.e.* $\hat{\varepsilon} \parallel [110]$ and $\mathbf{k} \parallel [\bar{1}10]$), the empty $e_g\ 3d_{x^2-y^2}$ is probed, thus leading to one peak in the E2 absorption cross section. The lp-DOS plots also enable to reveal the various hybridizations between the orbitals, which are involved in the pre-edge. Since MbCO is a molecule, these

hybridizations can be described in terms of molecular orbitals (MO). Let us first define the MO of the iron ligands, which are involved in the pre-edge. There are two axial ligands: the carbon atom of the CO molecule and the nitrogen atom of the H93 histidine group. The unoccupied MO orbitals of the CO molecule are π^* and σ^*, partially defined by the C $2p_x, p_y$ empty states and the C $2p_z$ empty states, respectively. One of the antibonding π^* MO of the histidine cycle is notably defined by the N_{his}-$2p_z$ empty states. In the heme plane, the four ligands are the N_p atoms, and it is the π^* MO of the porphyrin that participates in the pre-edge feature. The latter MO is partially described by the four N_p-$(2p_x, 2p_y)$ empty states. Then the ligand MOs are hybridized with the $3d$ empty states of iron to form other antibonding MO, which are at the origin of the pre-edge features. In particular, it can be seen in Fig. 6 (left) that the A_2 peak of the $\hat{\varepsilon} \perp$ *heme* configuration is due to E1 transitions $1s \rightarrow 4p_z$ where the Fe-$4p_z$ empty states are hybridized with the MOs formed by the t_{2g} $3d_{xz}$ and $-3d_{yz}$, and the π^* coming from CO. Consequently, the more the CO bond is tilted, *i.e.* the greater is the β angle, the more efficient is
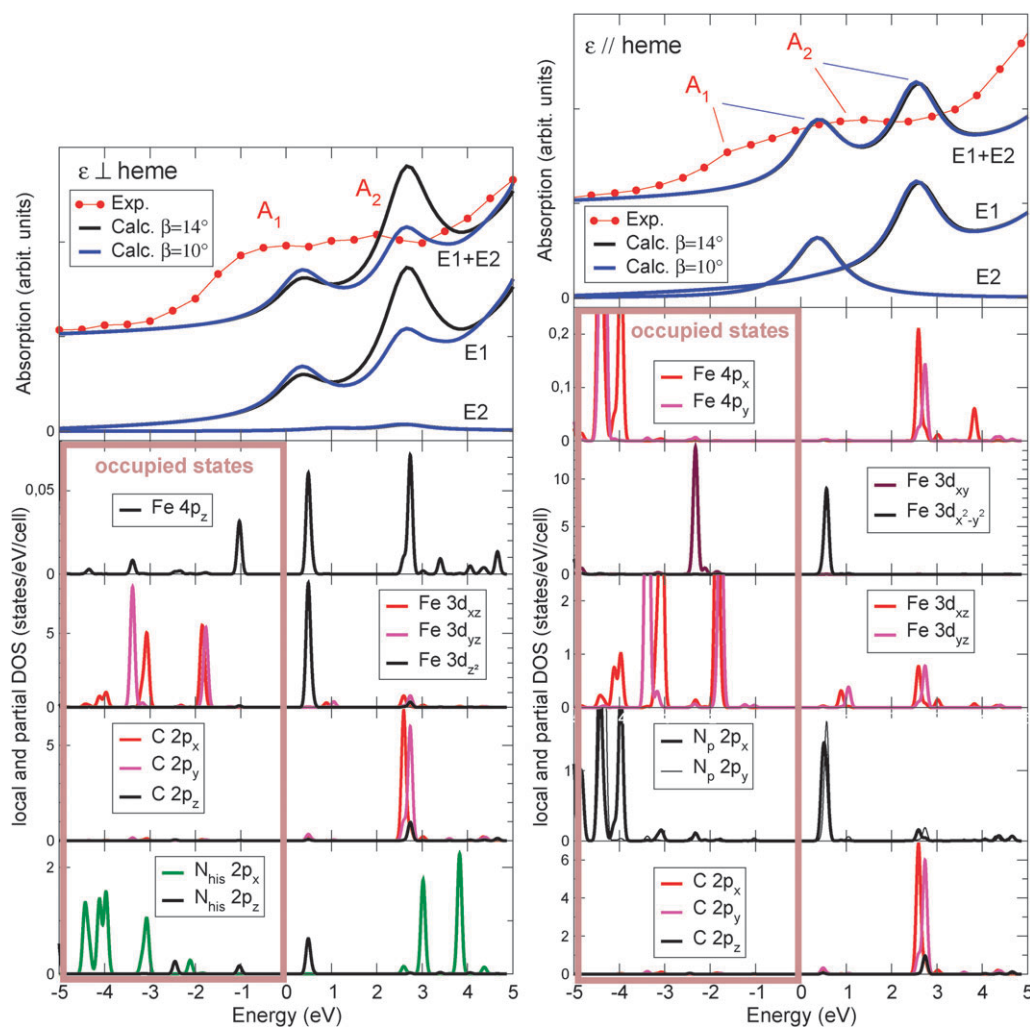
Fig. 6 Analysis of the MbCO pre-edge transitions for $\hat{\varepsilon}$ normal to the heme plane (left) and $\hat{\varepsilon}$ in the heme plane (right). Top panels: experimental and calculated pre-edge spectra for two values of the β angle (including the decomposition into E1 and E2 transitions). Bottom panels: local and partial DOS in the pre-edge region. The zero energy is the Fermi energy. The experimental spectra have been shifted in energy in order to make the main peak of the $\hat{\varepsilon} \perp$ *heme* polarized XANES experimental and theoretical spectra coincide.

Table 7 Main molecular orbital (MO) assignment of the A_1 and A_2 pre-edge features of the Fe K-XANES spectra of MbCO for two distinct orientations of the incident photon beam polarization ($\hat{\varepsilon}$), as deduced from single-particle lp-DOS and absorption cross-section calculations

Peak	Assignment for $\hat{\varepsilon} \perp heme$
A_1	E1: $1s \rightarrow 4p_z$ hybrid. with MO $[3d_{z^2} + \pi^*(H93)]^*$ and with MO $[3d_{z^2} + \sigma^*(CO)]^*$
A_2	E1: $1s \rightarrow 4p_z$ hybrid. with MO $[3d_{yz} - 3d_{xz} + \pi^*(CO)]^*$

Peak	Assignment for $\hat{\varepsilon} \parallel heme$
A_1	E2: $1s \rightarrow$ MO $[3d_{x^2-y^2} + \pi^*_{porph}]^*$
A_2	E1: $1s \rightarrow 4p_x, 4p_y$ hybrid. with MO $[3d_{xz}, 3d_{yz} + \pi^*(CO)]^*$

the hybridization. This explains why peak A_2 is more intense for $\beta = 14°$ than for $\beta = 10°$. Note that the $10°$ spectrum matches better with experiment. This result suggests that the $14°$, resulting from the fitting procedure of the XANES spectrum performed by Della Longa *et al.*,[34] is overestimated. The assignment of the pre-edge features for both orientations of the polarization vector in terms of unoccupied MO is given in Table 7. The lp-DOS calculations presented here partially confirm and complete the tentative MO assignments of the pre-edge features given by Della Longa *et al.*[48]

FeS$_2$-pyrite. Pyrite crystallizes in the cubic system and iron atoms are octahedrally coordinated to sulfur atoms sitting in four equivalent sites with point symmetry $\bar{3}$ (C_{3i}). Thus the iron site exhibits an inversion centre, which means that local p–d hybridization is forbidden: local E1 transitions are not expected in the pre-edge region. Consequently, only E2 transitions and non local E1 transitions can occur in the pre-edge region (as in the case of rutile). Note that in the pyrite cubic cell, the four FeS$_6$ octahedra are tilted from the cubic crystallographic axis by about $23°$.

The angular dependence of the Fe K pre-edge region of pyrite has been measured in order to reveal the E2 transitions.[50] Indeed, since the system is cubic, only the E2 transitions depend on the orientation of the crystal with respect to the X-ray beam, the E1 ones being isotropic.[29] The X-ray linear natural dichroism (XNLD) was found to be around 0.5% of the edge jump. Experimental results are compared with single-particle calculations in Fig. 7. A good agreement is obtained between theory and experiment for both the isotropic and XNLD spectra. The pre-edge is characterized by one main peak, containing two contributions, one E1 and one E2, as expected by symmetry considerations. The isotropic E2 contribution is about 4% of the pre-edge intensity and 0.7% of the edge jump. The pre-edge mainly arises from non-local E1 transitions (*i.e.* $1s \rightarrow p$ hybridized with $3d$-e_g states of the neighbouring Fe *via* the S p empty states). The ratio between the maximum intensity of the XNLD and the E2 isotropic contribution is found to be equal to 0.9. It was shown by performing complementary LFM calculations that this value strongly depends on the tilt angle of the FeS$_6$ octahedron:[50] this ratio decreases from 2.5, for a regular octahedron with its four-fold axis parallel to the z axis of the crystal (tilt angle equal to zero), to zero for a tilt angle equal to $30°$. Therefore,
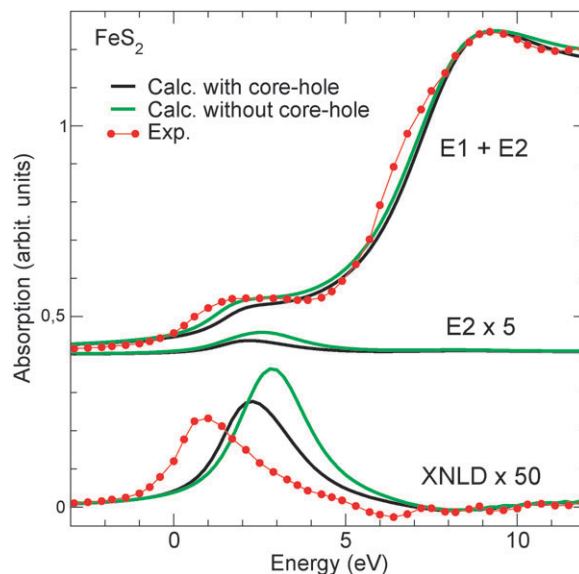
Fig. 7 Comparison between the experimental (red line with circles) XANES and XNLD spectra with the corresponding calculated spectra (in black, the potential including the $1s$ core-hole, and in green, the ground state potential). Note that the XNLD and the isotropic E2 contribution are multiplied by a factor 50 and 5, respectively.

in the latter geometrical configuration, no dichroic signal could be observed. Fig. 7 also shows the core-hole effects, which appear to be weak in the edge region. As in the case of rutile, we observe a shift of the E2 transitions towards lower energy when the core-hole is taken into account. However, this shift is not sufficient: the remaining energy difference between experimental and theoretical XNLD signal is 1.4 eV. This discrepancy illustrates again the difficulty of modelling the core-hole–electron interaction within the DFT-LDA approach.

3.3 Cr^{3+} K pre-edge

The K pre-edge of trivalent chromium is presented through three different examples of Cr-bearing minerals, where chromium substitutes for aluminium in octahedral position: Cr-doped spinel $MgAl_2O_4:Cr^{3+}$, emerald $Be_3Si_6Al_2O_{18}:Cr^{3+}$ and ruby α-$Al_2O_3:Cr^{3+}$. The amount of chromium being very low in these compounds (*e.g.*, below a few atomic-percent) the probability to have chromium atoms in neighbouring sites is also low. This enables us to exclude the contribution of non-local E1 transitions at the K pre-edge. The number of expected E2 transitions can be predicted for a d^3 configuration in octahedral environment, as can be seen from Fig. 8. The ground state of Cr^{3+} corresponds to a configuration where the three lowest d-orbitals (the t_{2g}-like) are occupied by the majority spin. In the excited state, the photoelectron can probe on the one hand the empty t_{2g} orbitals for minority spin (case B in Fig. 8), and on the other hand the empty e_g ones, for both majority and minority spins (cases A and C in Fig. 8, respectively). Therefore, three spin-polarized E2 transitions can be expected at the Cr K pre-edge. The sequence from spinel to ruby *via* emerald corresponds to a decreasing symmetry of the Cr-site, starting from the D_{3d} point group symmetry in Cr-spinel, to D_3 in emerald and finally C_3 in ruby. As will be shown, the degree of admixture between the empty p states
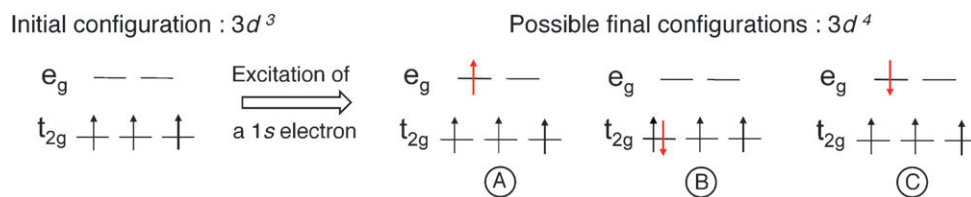
Fig. 8 Schematic monoelectronic representation of the 3d orbitals of Cr^{3+} in O_h symmetry for the ground state and the possible final states.

and the empty 3d states of the absorbing atom is consequently increasing, which affects the intensity of the local E1 transitions contributing to the pre-edge.

Cr-doped spinel $MgAl_2O_4$: Cr^{3+}. Spinel ($MgAl_2O_4$) is a cubic crystal with an $Fd\bar{3}m$ space group. Trivalent chromium can substitute for aluminium in the octahedral site. Upon substitution, the octahedral site retains its $\bar{3}m$ (D_{3d}) symmetry. Therefore, the chromium site exhibits an inversion symmetry: this implies that local E1 transitions cannot be expected and that the K pre-edge features should arise from E2 transitions only. In such a site symmetry, spherical tensor analysis predicts an angular dependence (XNLD) of the electric quadrupole absorption cross-section, when the absorption is measured on a single crystal. The full angular dependence was measured and modelled at the Cr K pre-edge by Juhin et al., in order to reveal quantitative information on the crystallographic and electronic structure of Cr^{3+}.[19]

The experimental spectra measured for two different orientations are shown in Fig. 9 (left and right). For each of them, the upper panel shows the experimental spectrum and the theoretical one, with the E1 and E2 contributions plotted separately. Both panels show that the Cr K pre-edge has a pure electric quadrupole character, as expected, since the E1 contribution contributes only to the edge tail without showing any features. For the two orientations ($\hat{\varepsilon}_a = [010]$, $\mathbf{k}_a = [\bar{1}00]$ and $\hat{\varepsilon}_b = [1, 1, \sqrt{2}]]$, $\mathbf{k}_b = [-1, -1, \sqrt{2}]$, respectively), the correct number of peaks (one and two, respectively) is well reproduced by the single-particle calculation. For the first configuration (Fig. 9, left), the experimental spectrum shows a single peak labelled A_1. The electric quadrupole operator, expressed as xy, enables to probe the empty d electronic density, projected on Cr, in the xy direction, i.e., between the Cr–O bonds. The corresponding empty d states have almost a pure t_{2g} character, and thus they can be reached only by a photoelectron with spin ↓ (Fig. 8, case B). This prediction is consistent with the calculation. For the second configuration (Fig. 9, right), two peaks A_1 and A_2 are obtained in the experimental pre-edge spectrum. For this orientation, the electric quadrupole operator is expressed as $\frac{3z^2-r^2}{4} - \frac{xy}{2}$, which enables to probe the 3d electronic density both in the xy and $3z^2-r^2$ directions. The corresponding d empty states are thus respectively t_{2g} and e_g ones. For the t_{2g} component, one peak is expected for spin ↓, as in the first configuration; for the e_g component, two peaks are expected, one for spin ↓ and one for spin ↑ (cases A and C in Fig. 8). These predictions are in line with the theoretical spectrum, which shows that peak A_1 arises from transitions towards $e_g\uparrow$ and $t_{2g}^\downarrow$ states, while peak A_2 corresponds to transitions towards $e_g\downarrow$ states. It should be mentioned that, although the symmetry of the Cr-site is D_{3d}, no splitting

between the empty t_{2g} orbitals is visible, which is an indication that the trigonal distortion is very small.

Although the agreement between theory and experiment is satisfactory enough to provide a clear vision of the assignment of the 1s-3d transitions occurring in the pre-edge, there are two main drawbacks. First, we observe again that in the calculation, the E2 pre-edge features occur at too high energy with respect to the edge, due to the modelling of the core-hole effects. Second, the absolute and the relative intensities are not perfectly reproduced using the single-particle approach, as well as the splitting of the two peaks, which is underestimated. This has been attributed to the fact that the interelectronic repulsion on the 3d levels of the Cr ion cannot fully be described in the LDA framework.[19]

Emerald $Be_3Si_6Al_2O_{18}$: Cr^{3+} and ruby α-Al_2O_3 : Cr^{3+}. As in the case of Cr-doped spinel, the Cr K pre-edge spectra measured on single crystals of emerald and ruby (with their three-fold axis perpendicular to the incident beam) display two features, A_1 and A_2 (see respectively Fig. 10 of ref. 20 and Fig. 3 of ref. 17). Single-particle calculations have revealed that both peaks are due to local E2 1s-3d transitions and local E1 1s-p transitions. The latter occur since the Cr-site is not centrosymmetric. Additionally, the amount of E1 transitions is higher in ruby, since the Cr site is more distorted than in emerald.[20] As beryl $Be_3Si_6Al_2O_{18}$ and corundum α-Al_2O_3 crystallize respectively in the $P6/mcc$ (D_{6h}^2) and $R\bar{3}2/c$ (D_{3d}^6) space groups, both E1 and E2 transitions show an angular dependence. For both compounds, the XNLD has been measured and fully interpreted using single-particle calculations. Moreover, the transitions observed in the different polarized XANES spectra are in line with the predictions made through group theory, provided the character tables of the D_3 and C_3 symmetry groups is used.

3.4 V^{3+} K pre-edge

The vanadium K pre-edge was studied through the example of tsavorite $Ca_3Al_2(SiO_4)_3$:V^{3+}, a V-bearing grossular. Tsavorite is a garnet and therefore crystallizes in the cubic system with space group $Ia\bar{3}d$. Vanadium is present as a substituted minor element in the Al site, with $\bar{3}$ (C_{3i}) point symmetry. Hence, neither local nor non-local E1 transitions are expected: only E2 transitions contribute to the pre-edge region. These E2 transitions can probe t_{2g} and e_g states whatever the spin is up or down. As explained in the case of spinel, the expression of the E2 cross-section predicts an angular dependence of the pre-edge when the crystal orientation is varied with respect to the incident X-ray beam.[29] Polarized XANES spectra at the V K-edge were recorded on an oriented single-crystal by

5628 | *Phys. Chem. Chem. Phys.*, 2010, **12**, 5619–5633

This journal is © the Owner Societies 2010
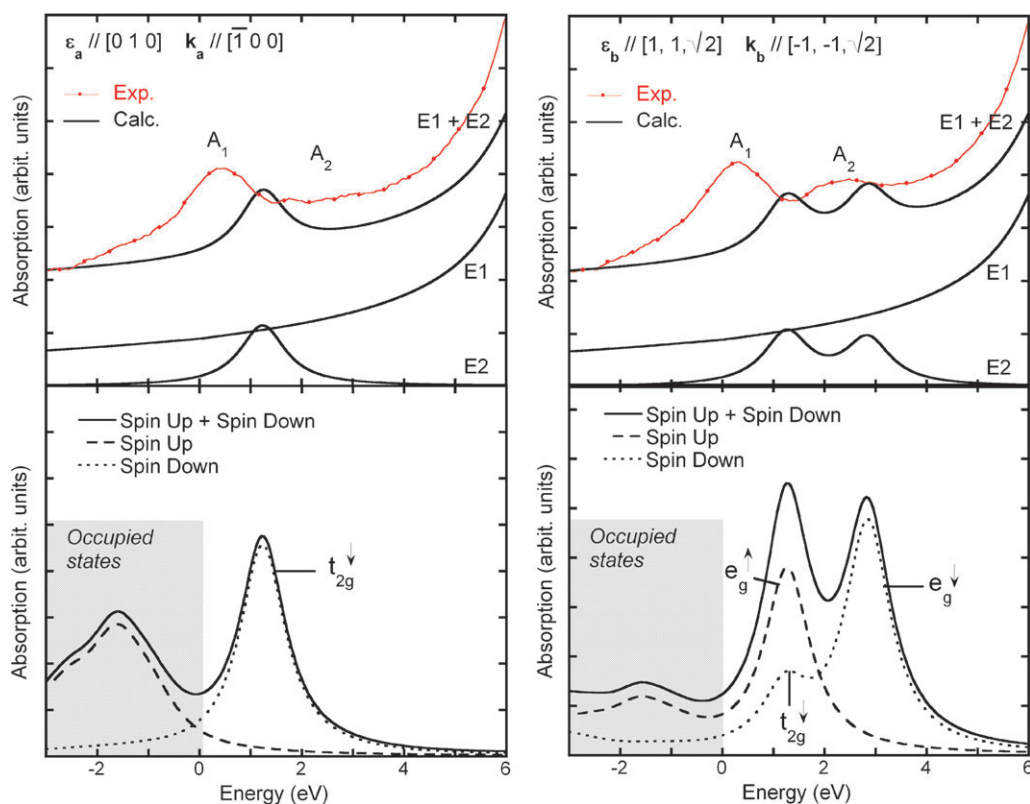
Fig. 9 Analysis of the K pre-edge transitions of Cr^{3+} in spinel, for the ($\hat{\varepsilon}_a = [010]$; $\mathbf{k_a} = [\bar{1}00]$) orientation (left), and for the ($\hat{\varepsilon}_b = [1, 1, \sqrt{2}]$; $\mathbf{k_b} = [-1, -1, \sqrt{2}]$) orientation (right). Top panels: experimental and calculated pre-edge spectra, with the decomposition into E1 and E2 transitions. Bottom panels: spin-polarized calculations of the E2 cross-section. The zero energy is the Fermi energy. The grey region corresponds to the virtual transitions towards the occupied states. The experimental spectra have been shifted in energy in order to make the main peak of the edge coincide with the theoretical data.

Bordage *et al.*[21] The recorded orientations are identical to those measured for Cr-bearing spinel.

The upper panels of Fig. 10 (left and right) compare the experimental and theoretical spectra obtained for the two orientations $\hat{\varepsilon}_a = [010]$; $\mathbf{k_a} = [\bar{1}00]$ and $\hat{\varepsilon}_b = [1, 1, \sqrt{2}]$; $\mathbf{k_b} = [-1, -1, \sqrt{2}]$. For both orientations, the pre-edge exhibits three well-defined structures, which are well reproduced by the single-particle calculations, but again at too high energy. The pure electric quadrupole character of the pre-edge is well-observed, since the E1 contribution presents no structure in the pre-edge region and contributes only to the edge tail. When superimposing the spectra of each orientations, one notices that the expected angular dependence of the pre-edge is satisfactorily reproduced by the calculations.[21] Indeed, both the relative energies and intensities are correctly calculated.

The lower panels of Fig. 10 (left and right) show the spin-polarized calculations of the E2 cross-section performed for each experimental orientation. An assignment of the E2 transitions involved in the experimental peaks, labelled A_1, A_2 and A_3, can be done within a single-particle view of the transitions from the 1s states to the empty 3d ones. Peak A_1 is thus attributed to transitions towards the $t_{2g}^{\uparrow}$ states. Peak A_2 arises from two contributions: transitions towards the $t_{2g}^{\downarrow}$ and $e_g^{\uparrow}$ states. Peak A_3 is attributed to transitions towards the $e_g^{\downarrow}$ states. The simple picture of the transitions involved in the V^{3+} K pre-edge in tsavorite enables to understand the spectral features observed on the experimental spectra. However, a

more detailed attention must be paid to peak A_1 since it is situated astride the occupied and empty states. This is due to the $3d^2$ electronic configuration of V^{3+}: two t_{2g} orbitals are occupied and one is empty. The occupied states represented in Fig. 10 (lower panels) correspond to virtual transitions towards these occupied orbitals. Real transitions can occur towards the empty t_{2g} orbital. The spectrum should thus display two well-separated peaks, the first in the occupied states and the second in the empty states. Nevertheless, the empty and occupied t_{2g} orbitals are too close in energy for the single-particle DFT approach to reproduce their splitting into two separated components, as expected by the irreducible representations of the C_{3i} vanadium site point group. Consequently, even if the agreement between experiment and calculation is quite satisfactory when the occupied states are cut, standard plane-wave DFT approach fails to properly model 3d incomplete spin-polarized shells. This drawback will be again illustrated with the following and last compound.

3.5 Low-spin Fe^{3+} K-edge

Cyanomet-myoglobin (MbCN). The case of MbCN conjugates the difficulties of the two previous cases: the Cr K pre-edge for the majority spin and the V K pre-edge for the minority spin. Indeed the presence of CN in the sixth position of the Fe coordinates confers to the Mb protein a $S_z = 1/2$ spin state, with Fe in a trivalent low-spin state as schematized

This journal is © the Owner Societies 2010

Phys. Chem. Chem. Phys., 2010, **12**, 5619–5633 | 5629
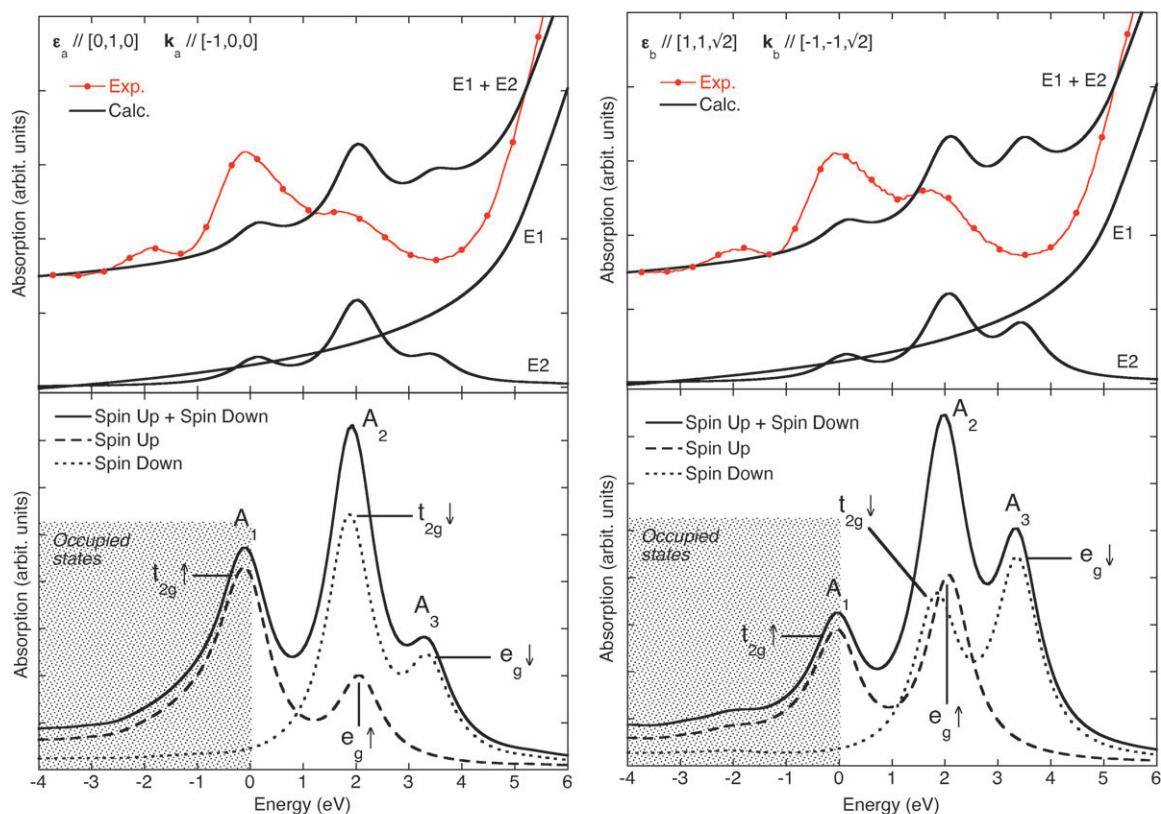
Fig. 10 Analysis of the K pre-edge transitions of V^{3+} in tsavorite, for the ($\hat{\varepsilon}_a = [010]$; $\mathbf{k}_a = [\bar{1}00]$) orientation (left) and for the ($\hat{\varepsilon}_b = [1, 1, \sqrt{2}]$; $\mathbf{k}_b = [1, 1, \sqrt{2}]$) orientation (right). Top panels: experimental and calculated pre-edge spectra, with the decomposition into E1 and E2 transitions. Bottom panel: spin-polarized calculations of the E2 cross-section. The zero energy is the Fermi energy. The grey region corresponds to the virtual transitions towards the occupied states. The experimental spectra have been shifted in energy in order to make the main peak of the edge coincide with the theoretical data.

in Fig. 1e. The geometry around Fe is quite similar to that of MbCO, meaning that the same kinds of electronic transitions are expected in the pre-edge region, *i.e.*, E2 and local E1. For the E2 part, three different transitions can be expected (Fig. 1), *i.e.* to t_{2g} states for minority spin, and to e_g states, for both majority and minority spins.

The top panels of Fig. 11 (left and right) compare the experimental Fe K pre-edge polarized spectra of MbCN with cross-section calculations (for $\hat{\varepsilon} \perp$ *heme* and $\hat{\varepsilon} \parallel$ *heme*, respectively). The spectra were recorded by Arcovito *et al.*,[35] applying a protocol similar to that used for MbCO.[48] While the pre-edge spectra MbCO show two features, the experimental pre-edge spectra of MbCN are characterized by one main peak, labelled A, which is twice as more intense for $\hat{\varepsilon} \perp$ *heme* than for $\hat{\varepsilon} \parallel$ *heme*. The shape and the anisotropy of the Fe K pre-edge of MbCN is well reproduced by the single-particle calculations (the fact that the calculated pre-edges are too intense with respect to experiment is essentially due to a too weak γ broadening parameter used in the cross-section calculation). The decomposition into E1 and E2 contributions shows that peak A is due to E1 transitions for $\hat{\varepsilon} \perp$ *heme* and to E2 transitions for $\hat{\varepsilon} \parallel$ *heme*. The same decomposition has been observed for peak A_1 of MbCO. Since Fe lies in a nearly centrosymmetric environment within the heme plane, the absence of local E1 transitions for $\hat{\varepsilon} \parallel$ *heme* then makes sense.

Although the expected number of pre-edge components is four (three E2 and one E1), one observes only one single broad feature in the XANES spectrum, which can be explained by the spin-polarized lp-DOS of Fe and of its neighbours (lower panels of Fig. 11). This is due to several reasons. First, because of the experimental configurations chosen, the transitions towards the partially empty t_{2g} states cannot be probed. Second, as can be seen from the lp-DOS, no significant energy splitting is observed between minority and majority spins: the transitions to the empty e_g states thus occur at a similar energy for both spins. Third, the local E1 transitions occur at an energy, which is close to the one of the E2 transitions (about 2.5 eV *vs.* 2.0 eV above the Fermi level, respectively).

These lp-DOS show that peak A has the same assignment as peak A_1 of MbCO for both orientations. Indeed, the same MOs are involved at the energy of the calculated A peak plotted in the top panels. Hence, for the $\hat{\varepsilon} \perp$ *heme* orientation, peak A is due to transitions $1s \rightarrow 4p_z$ where the $4p_z$ orbital is hybridized with the MOs $[3d_{z^2} + \sigma^*(CN)]^*$ and $[3d_{z^2} + \pi^*(H93)]^*$ (the $\sigma^*(CN)$ and $\pi^*(H93)$ MO being displayed by the C $2p_z$ lp-DOS and the N$_{his}$ $2p_z$ lp-DOS). For the $\hat{\varepsilon} \parallel$ *heme* orientation, peak A is due to transitions $1s \rightarrow 3d_{x^2-y^2}$ where the Fe $3d_{x^2-y^2}$ orbital participates in the MO $[3d_{x^2-y^2} + \pi^*_{porph}]$ (the π^*_{porph} MO is illustrated by the $2p_x$ and $2p_y$ partial DOS of the N atoms belonging to the heme plane).
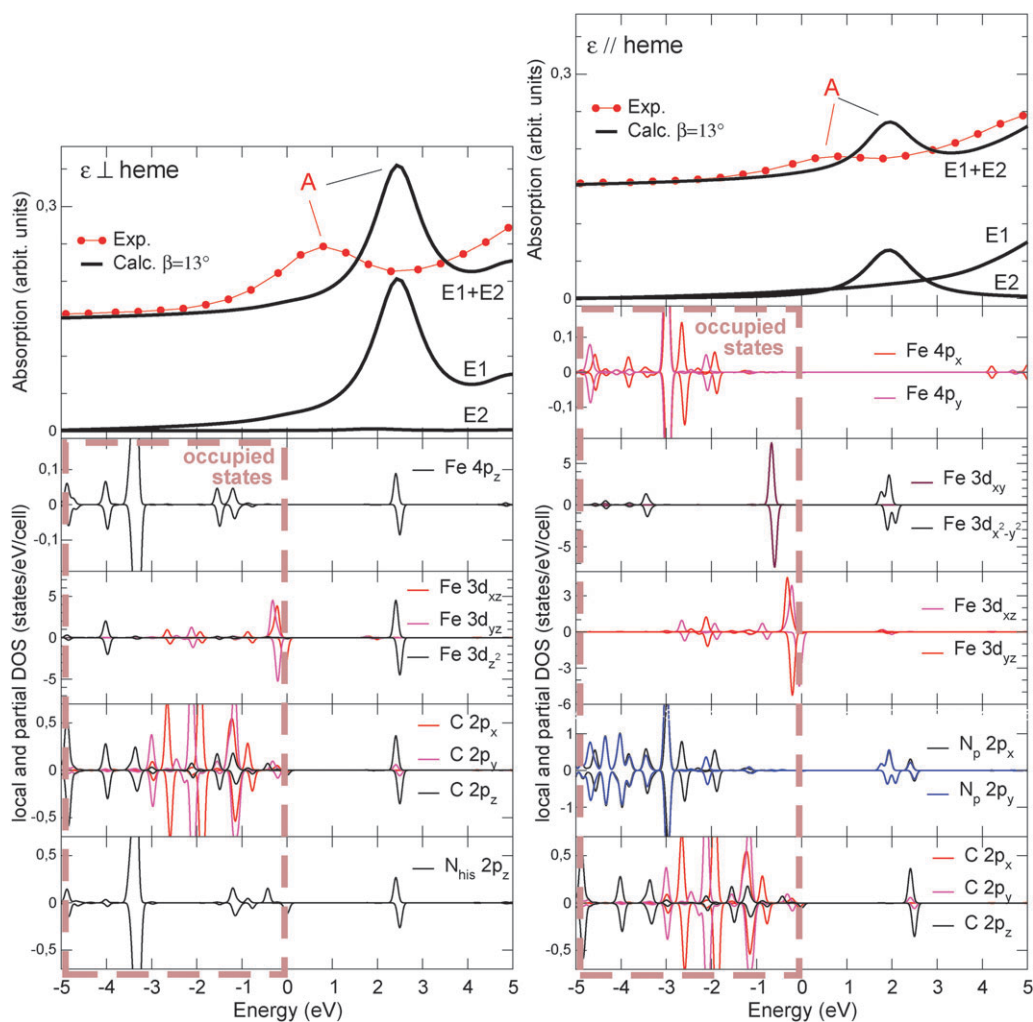
Fig. 11 Analysis of the MbCN pre-edge transitions for $\hat{\varepsilon}$ normal to the heme plane (left) and $\hat{\varepsilon}$ in the heme plane (right). Top panels: experimental and calculated pre-edge spectra (including the decomposition into E1 and E2 transitions). Bottom panels: local and partial spin-polarized DOS involved in the pre-edge region. The lp-DOS of majority spin (resp. minority spin) are displayed with positive values of states/eV/cell (resp. with negative values). The zero energy is the Fermi energy. The experimental spectra have been shifted in energy in order to make the main peak of the $\hat{\varepsilon} \perp$ *heme* polarized XANES experimental and theoretical spectra coincide.

Apart from the now well-known energy position problem of single-particle calculations, the pre-edge of MbCN appears not so critical to model (as initially expected). Nevertheless, these calculations reveal a failure similar to that observed in the case of tsavorite, *i.e.*, the absence of energy splitting of the spin ↓ partially filled t_{2g} shell. Indeed the Fermi energy, as calculated by the plane-wave DFT code, is found to be at the middle of the main peak of the spin ↓ Fe $3d_{xz}$ density of states (see the corresponding panels of Fig. 11). Fortunately, this problem has no incidence on the cross-section calculations because the Fe $3d_{xz}$ states are not probed in the orientation chosen in the experimental setup.

4. Conclusion

In this paper, we have presented a detailed investigation of the K pre-edge of 3d elements in several compounds. Through these examples, the issue of coupling closely experiment and theory to extract electronic and structural information was emphasized. In all the compounds investigated, single-particle calculations were able to reproduce satisfactorily the experimental pre-edge: the number of peaks was well reproduced, and the relative energy positions and relative intensities were in good agreement with the experimental data. This has allowed the interpretation of the experimental features within a monoelectronic view of the transitions involved in the K pre-edge. The information that can be directly inferred from such an assignment are the electric dipole or electric quadrupole character of the transitions, as well as the degree of local and non-local orbital hybridization. By taking advantage of XNLD to probe specific empty orbitals, it is possible to draw a picture orientated in space. In all cases, the angular dependence of the K pre-edge was indeed reproduced in a level, which was good enough to allow its interpretation. Moreover, if some $[\hat{\varepsilon}, \mathbf{k}]$ orientations of the crystal with respect to the X-ray beam are not accessible experimentally, calculations are the only way to probe the corresponding empty levels. Within such a detailed analysis, the electronic structure of a transition metal

ion in a given local environment can be well understood and therefore, its spectral signature well characterized.

However, single-particle calculations show some limitations. In the case of spin-polarized calculations for transition metal ions with incomplete d shells (V^{3+} and LS Fe^{3+}), occupied and empty states are not well separated in the calculation. Such systems represent a real challenge for DFT. However, we point out that the assignment of the XANES features in terms of monoelectronic transitions still remains possible, provided that one keeps in mind that the $3d$ shells are incomplete. In all the compounds investigated, the calculation of K pre-edge spectra within DFT suffers from two main drawbacks, i.e., the modelling of the core-hole interaction, on one hand, and the $3d$ electron–electron repulsion, on the other hand.

First, for all the compounds presented in this paper, we found out that the E2 and local E1 transitions are systematically calculated at a too high energy with respect to the edge. This effect is due to the modelling of the $1s$ core-hole–electron interaction, which leads to an overestimation of the screening of the $1s$ core-hole. The relative energy positions of the pre-edge features can be improved mainly by two means. The simplest way consists of considering a core-hole with a positive charge superior to one, in order to increase artificially its attraction on the $3d$ empty states. Nevertheless, such calculations cannot be considered as ab initio anymore, since the value of the core-hole is a fitted parameter. An alternative, more elegant way is to consider a dynamic core-hole, instead of a static one as in the calculations presented here. This requires the Bethe–Salpeter formalism, which treats electron and hole dynamics ab initio, as well as electron–hole interactions.[51] However, such calculations are nowadays still time-consuming, and complex systems like doped minerals and proteins are definitely challenging.

Second, the other main drawback of single-particle calculations is the modelling of electronic interactions: LDA and GGA approximations give indeed a description of these interactions in a mean-field way, which is not therefore completely satisfactory and which can be responsible for the possible differences in relative peak positions and intensities, compared to experiment. However, keeping in mind that the pre-edge features correspond to localized empty states where $3d$–$3d$ interactions are relevant, one must admit that DFT-LDA or DFT-GGA approaches already enable a good modelling of the angular dependence of the pre-edge. In the case of tsavorite, XNLD was very well-reproduced quantitatively. The less satisfactory agreement was observed for Cr-doped spinel, but it did not hamper the interpretation of the pre-edge. In certain cases, the description of $3d$–$3d$ electronic repulsion can be improved by performing LDA+ U (or GGA + U) calculations. The Hubbard parameter $U(3d)$ corresponds to the $3d$ Coulombian "on-site" repulsion and measures the spurious curvature of the energy functional as a function of occupation. The Hubbard parameter can be determined self-consistently using the Quantum-Espresso code, as an intrinsic linear-response property of the system.[52,53] Nevertheless, DFT + U calculations cannot be performed for all systems, since the number of spins up and spins down needs to be non-zero.[52] Only a few XANES calculations have been performed in DFT + U, i.e., Ni K-edge in NiO, Cu K-edge in

CuO and La_2CuO_4 and Co K-edge in $LiCoO_2$.[22,23,54] In these compounds, the addition of U, combined to the core-hole effects, has enabled to shift the local E2 transitions from the non-local E1 ones in the pre-edge, yielding a better agreement between calculations and experiments.

The way to take into account the many-body interactions lacking in DFT-LDA (i.e., the multi-Slater determinant nature of the electronic states) is to use the multiplet approach. For example, in the case of Cr-doped spinel, it has been shown that the angular dependence of the K pre-edge could be better modelled.[19] However, this approach has also some drawbacks: (i) it uses a local approach, where a single transition metal ion is considered as embedded in a ligand field. Therefore, non-local E1 transitions occurring in the pre-edge cannot be calculated, (ii) because the calculation includes multiplet effects, a simple atomic picture is no longer possible to assign the transitions in terms of monoelectronic transitions, (iii) it uses some empirical parameters, which may not be available for all the systems. Hence, multiplet and single-particle methods must be considered as highly complementary. The development of approaches that go beyond DFT, such as DFT-CI (Configuration Interaction), TD-DFT and Bethe–Salpeter opens new prospects to draw a fully ab initio picture of the pre-edge structure. A nice success of TD-DFT is already illustrated by the case of K pre-edge of Fe^{2+} and Fe^{3+} in molecular model complexes.[26] The application of these methods to more complex systems such as crystals requires developments, which are now under progress.

Acknowledgements

References

1 T. Yamamoto, X-Ray Spectrom., 2008, **37**, 572–584.
2 L. Galoisy, G. Calas and M.-A. Arrio, Chem. Geol., 2001, **174**, 307–319.
3 M. Wilke, F. Farges, P.-E. Petit, G. E. Brown Jr. and F. Martin, Am. Mineral., 2001, **86**, 714–730.
4 F. Farges, Phys. Chem. Miner., 2009, **36**, 463–481.
5 S. R. Sutton, J. Karner, J. Papike, J. S. Shearer, M. Newville, P. Eng, M. Rivers and M. D. Dyar, Geochim. Cosmochim. Acta, 2005, **69**, 2333–3348.
6 E. Balan, J. P. R. de Villiers, S. G. Eeckhout, P. Glatzel, M. J. Toplis, E. Fritsch, T. Allard, L. Galoisy and G. Calas, Am. Mineral., 2006, **91**, 953–956.
7 A. Bordage, PhD thesis, Université Pierre et Marie Curie, Paris 6, 2009.

8 F. M. F. de Groot, *X-ray Absorption Fine Structure-XAFS13*, 2007, pp. 37–43.

9 T. E. Westre, P. Kennepohl, J. G. DeWitt, B. Hedman, K. O. Hodgson and E. I. Solomon, *J. Am. Chem. Soc.*, 1997, **119**, 6297–6314.

10 M.-A. Arrio, S. Rossano, C. Brouder, L. Galoisy and G. Calas, *Europhys. Lett.*, 2000, **51**, 454–460.

11 F. de Groot, G. Vankò and P. Glatzel, *J. Phys.: Condens. Matter*, 2009, **21**, 104207.

12 Y. Joly, *Phys. Rev. B: Condens. Matter Mater. Phys.*, 2001, **63**, 125120–125129.

13 Y. Joly, D. Cabaret, H. Renevier and C. R. Natoli, *Phys. Rev. Lett.*, 1999, **82**, 2398.

14 A. L. Ankudinov, B. Ravel, J. J. Rehr and S. D. Conradson, *Phys. Rev. B: Condens. Matter Mater. Phys.*, 1998, **58**, 7565–7576.

15 F. Farges, *Phys. Rev. B: Condens. Matter Mater. Phys.*, 2005, **71**, 155109.

16 T. Yamamoto, T. Mizoguchi and I. Tanaka, *Phys. Rev. B: Condens. Matter Mater. Phys.*, 2005, **71**, 245113.

17 E. Gaudry, D. Cabaret, P. Sainctavit, C. Brouder, F. Mauri, A. Rogalev and J. Goulon, *Phys. Scr.*, 2005, 191–192.

18 D. Cabaret, B. Couzinet, A.-M. Flank, J.-P. Itié, P. Lagarde and A. Polian, *AIP Conf. Proc.*, 2007, **882**, 120–122.

19 A. Juhin, C. Brouder, M.-A. Arrio, D. Cabaret, P. Sainctavit, E. Balan, A. Bordage, A. P. Seitsonen, G. Calas, S. G. Eeckhout and P. Glatzel, *Phys. Rev. B: Condens. Matter Mater. Phys.*, 2008, **78**, 195103.

20 E. Gaudry, D. Cabaret, C. Brouder, I. Letard, A. Rogalev, F. Wilhlem, N. Jaouen and P. Sainctavit, *Phys. Rev. B: Condens. Matter Mater. Phys.*, 2007, **76**, 094110.

21 A. Bordage, C. Brouder, E. Balan, D. Cabaret, A. Juhin, M.-A. Arrio, P. Sainctavit, G. Calas and P. Glatzel, *Am. Mineral*, submitted.

22 C. Gougoussis, M. Calandra, A. P. Seitsonen, C. Brouder, A. Shukla and F. Mauri, *Phys. Rev. B: Condens. Matter Mater. Phys.*, 2009, **79**, 045118.

23 C. Gougoussis, M. Calandra, A. Seitsonen and F. Mauri, *Phys. Rev. B: Condens. Matter Mater. Phys.*, 2009, **80**, 075102.

24 G. Onida, L. Reining and A. Rubio, *Rev. Mod. Phys.*, 2002, **74**, 601–659.

25 R. de Francesco, M. Stener, M. Causà, D. Toňoliac and G. Fronzoni, *Phys. Chem. Chem. Phys.*, 2006, **8**, 4300–4310.

26 S. D. George, T. Petrenko and F. Neese, *J. Phys. Chem. A*, 2008, **112**, 12936–12943.

27 E. L. Shirley, *J. Electron Spectrosc. Relat. Phenom.*, 2004, **136**, 77–83.

28 J. C. Woicik, E. L. Shirley, C. S. Hellberg, K. E. Andersen, S. Sambasivan, D. A. Fischer, B. D. Chapman, E. A. Stern, P. Ryan, D. L. Ederer and H. Li, *Phys. Rev. B: Condens. Matter Mater. Phys.*, 2007, **75**, 140103.

29 C. Brouder, *J. Phys.: Condens. Matter*, 1990, **2**, 701–738.

30 P. Blaha, K. Schwarz, P. Sorantin and S. B. Trickey, *Comput. Phys. Commun.*, 1990, **59**, 399.

31 M. Taillefumier, D. Cabaret, A.-M. Flank and F. Mauri, *Phys. Rev. B: Condens. Matter Mater. Phys.*, 2002, **66**, 195107.

32 D. Cabaret, E. Gaudry, M. Taillefumier, P. Sainctavit and F. Mauri, *Phys. Scr.*, 2005, 131–133.

33 A. Juhin, G. Calas, D. Cabaret, L. Galoisy and J.-L. Hazemann, *Phys. Rev. B: Condens. Matter Mater. Phys.*, 2007, **76**, 054105.

34 S. Della Longa, A. Arcovito, M. Girasole, J.-L. Hazemann and M. Benfatto, *Phys. Rev. Lett.*, 2001, **87**, 155501.

35 A. Arcovito, M. Benfatto, M. Cianci, S. S. Hasnain, K. Nienhaus, G. U. Nienhaus, C. Savino, R. W. Strange, B. Vallone and S. Della Longa, *Proc. Natl. Acad. Sci. U. S. A.*, 2007, **104**, 6211–6216.

36 B. Pfrommer, D. Raczkowski, A. Canning, S. G. Louie and (Lawrence Berkeley National Laboratory, with contributions from F. Mauri, M. Cote, Y. Yoon, Ch. Pickard and P. Haynes), PARAllel Total Energy Code, www.nersc.gov/projects/paratec.

37 P. Gianozzi, S. Baroni, N. Bonini, M. Calandra, R. Car, C. Cavazzoni, D. Ceresoli, G. Chiarotti, M. Cococcioni, I. Dabo, A. D. Corso, S. de Gironcoli, R. Gebauer, U. Gerstmann, C. Gougoussis, A. Kokalj, M. Lazzeri, L. M. S. Colomer, N. Marzari, F. Mauri, S. Paolini, A. Pasquarello, L. Paulatto, C. Sbraccia, S. Scandolo, G. Sclauzero, A. Seistsonen, A. Smogunov, P. Umari and R. Wentzcovitch, *J. Phys.: Condens. Matter*, 2009, **21**, 395502.

38 N. Troullier and J. Martins, *Phys. Rev. B: Condens. Matter*, 1991, **43**, 1993–2006.

39 L. Kleinman and D. Bylander, *Phys. Rev. Lett.*, 1982, **48**, 1425–1428.

40 B. Poumellec, R. Cortes, G. Tourillon and J. Berthon, *Phys. Status Solidi B*, 1991, **164**, 319–326.

41 P. L. Fèvre, H. Magnan, D. Chandesris, J. Jupille, S. Bourgeois, A. Barbier, W. Drube, T. Uozumi and A. Kotani, *Nucl. Instrum. Methods Phys. Res., Sect. A*, 2005, **547**, 176–186.

42 O. Durmeyer, E. Beaurepaire, J. P. Kappler, C. Brouder and F. Baudelet, *J. Phys. Condens. Matter*, 2010, **22**, 125504.

43 C. Brouder and D. Cabaret, *Phys. Rev. B*, 2010, **81**, 115125.

44 M. F. Ruiz-Lopez and A. Muñoz-Páez, *J. Phys.: Condens. Matter*, 1991, **3**, 8981–8990.

45 P. Glatzel, M. Sikora and M. Fernandez-García, *Eur. Phys. J. Spec. Top.*, 2009, **169**, 207–214.

46 G. S. Kachalova, A. N. Popov and H. D. Bartunik, *Science*, 1999, **284**, 473–476.

47 J. Vojtechovsky, K. Chu, J. Berendzen, R. M. Sweet and I. Schlichting, *Biophys. J.*, 1999, **77**, 2153–2174.

48 S. Della Longa, A. Arcovito, B. Vallone, A. Congiu Castellano, R. Kahn, J. Vicat, Y. Soldo and J.-L. Hazemann, *J. Synchrotron Radiat.*, 1999, **6**, 1138–1147.

49 D. Cabaret, S. Della Longa, M. Arfaoui, F. Mauri, unpublished.

50 D. Cabaret, C. Brouder, M. A. Arrio, P. Sainctavit, Y. Joly, A. Rogalev and J. Goulon, *J. Synchrotron Radiat.*, 2001, **8**, 460–462.

51 E. L. Shirley, *Phys. Rev. Lett.*, 1998, **80**, 794.

52 M. Cococcioni and S. de Gironcoli, *Phys. Rev. B: Condens. Matter Mater. Phys.*, 2005, **71**, 035105.

53 H. J. Kulik, M. Cococcioni, D. A. Scherlis and N. Marzari, *Phys. Rev. Lett.*, 2006, **97**, 103001.

54 A. Juhin, F. de Groot, G. Vankó, M. Calandra and C. Brouder, *Phys. Rev. B*, 2010, **81**, 115115.

55 C. J. Howard, T. M. Sabine and F. Dickson, *Acta Crystallogr., Sect. B: Struct. Sci.*, 1991, **47**, 462–468.

56 E. D. Stevens, M. L. DeLucia and P. Coppens, *Inorg. Chem.*, 1980, **19**, 813–820.

57 T. Yamanaka and Y. Takeuchi, *Z. Kristallogr.*, 1983, **165**, 65–78.

58 C. Geiger and T. Armbruster, *Am. Mineral.*, 1997, **82**, 740–747.

59 J. P. Perdew, S. Burke and M. Ernzerhof, *Phys. Rev. Lett.*, 1996, **77**, 3865.

60 D. M. Ceperley and B. J. Alder, *Phys. Rev. Lett.*, 1980, **45**, 566–569.

61 A. Kokalj, *Comput. Mater. Sci.*, 2003, **28**, 155–168.

This journal is © the Owner Societies 2010

Phys. Chem. Chem. Phys., 2010, **12**, 5619–5633 | 5633